Single-molecule spectroscopy of protein conformational dynamics in live eukaryotic cells

Iwo König[1,3], Arash Zarrine-Afsar[1–3], Mikayel Aznauryan[1–3], Andrea Soranno[1], Bengt Wunderlich[1], Fabian Dingfelder[1], Jakob C Stüber[1], Andreas Plückthun[1], Daniel Nettels[1] & Benjamin Schuler[1]

Single-molecule methods have become widely used for quantifying the conformational heterogeneity and structural dynamics of biomolecules *in vitro*. Their application *in vivo*, however, has remained challenging owing to shortcomings in the design and reproducible delivery of labeled molecules, the range of applicable analysis methods, and suboptimal cell culture conditions. By addressing these limitations in an integrated approach, we demonstrate the feasibility of probing protein dynamics from milliseconds down to the nanosecond regime in live eukaryotic cells with confocal single-molecule Förster resonance energy transfer (FRET) spectroscopy. We illustrate the versatility of the approach by determining the dimensions and submicrosecond chain dynamics of an intrinsically disordered protein; by detecting even subtle changes in the temperature dependence of protein stability, including in-cell cold denaturation; and by quantifying the folding dynamics of a small protein. The methodology opens possibilities for assessing the effect of the cellular environment on biomolecular conformation, dynamics and function.

Advances in methodology are making it gradually more feasible to investigate biomolecular processes in their native cellular environment. The ultimate goal is to reach quantitative molecular understanding with the same rigor as in test-tube experiments. Owing to its sensitivity, fluorescence has become particularly popular—especially with the broad availability of fluorescent proteins[1]—for investigating cellular localization, biomolecular interactions[2], and protein stability and folding dynamics[3] in living cells. This sensitivity has enabled the use of single-molecule tracking[4,5], intracellular fluorescence correlation spectroscopy (FCS)[6], and image correlation methods[7] for investigating molecular diffusion and transport processes. Super-resolution methods now enable localization and dynamic imaging below the diffraction limit in live cells[8,9]. In prokaryotic cells, substantial progress has recently been reported for single-molecule detection *in vivo*, including the investigation of stochasticity in gene expression[10] and the mechanisms of DNA replication[11] and repair[12], for example, in combination with electroporation of labeled molecules[13]. The first single-molecule FRET experiments for detecting conformational changes of proteins in live eukaryotic cells have also been reported[14]. However, in spite of these advances, the use of single-molecule spectroscopy for resolving the subnanometer conformational changes of biomolecules and especially the wide range of relevant timescales has remained challenging *in vivo*.

This challenge largely originates from the multifactorial requirements for successful in-cell single-molecule measurements, such as (i) the cellular host system needs to be prepared in a fashion that minimizes autofluorescence; (ii) suitable excitation wavelengths and FRET dyes are needed that optimize molecular brightness of the sample compared to cellular background; (iii) the sample needs to be delivered into the cell in a targeted and reproducible fashion at the low concentrations suitable for single-molecule detection; (iv) measurements must follow sample delivery promptly enough to allow the dynamics of cellular targeting and localization to be followed and to avoid intracellular sample degradation; (v) intact cellular activity must be preserved and controlled for; (vi) both immobile and freely diffusing molecules should be detectable; and (vii) data analysis must make optimal use of the limited reservoir of molecules per cell to enable access to submillisecond timescales.

Here we show that with an integrated approach optimizing the points listed above, a surprisingly broad spectrum of confocal single-molecule FRET and nanosecond FCS methods that have previously been limited to *in vitro* experiments[15–18] could be used in live eukaryotic cells. As a result, even small conformational changes of protein molecules and conformational dynamics down to the nanosecond range became accessible in in-cell experiments. To illustrate the potential of the methodology, we investigated, in live cells, (i) the conformational distributions and nanosecond dynamics of an intrinsically disordered protein (IDP); (ii) the changes in the temperature-dependent conformational stability of a protein, including its cold denaturation; and (iii) the millisecond kinetics of a protein-folding reaction.

[1]Department of Biochemistry, University of Zurich, Zurich, Switzerland. [2]Present addresses: Techna Institute for the Advancement of Technology for Health, University Health Network, University of Toronto, Toronto, Ontario, Canada (A.Z.-A.); Keenan Research Centre for Biomedical Science, St. Michael's Hospital, Toronto, Ontario, Canada (A.Z.-A.); Interdisciplinary Nanoscience Center, Aarhus University, Aarhus, Denmark (M.A.). [3]These authors contributed equally to this work. Correspondence should be addressed to B.S. (schuler@bioc.uzh.ch).

RECEIVED 27 JANUARY; ACCEPTED 22 MAY; PUBLISHED ONLINE 6 JULY 2015; DOI:10.1038/NMETH.3475

RESULTS

In-cell confocal single-molecule FRET spectroscopy

Among the main considerations for performing intracellular single-molecule spectroscopy are, one, the reduction of cellular autofluorescence to a level that does not interfere with single-molecule detection and, two, the targeted application of labeled molecules into cells[5,10,19]. Autofluorescence in the visible wavelength range tends to decrease with increasing excitation wavelength[20], and above ~520 nm, autofluorescence of many cell lines is already sufficiently low. We chose to work with recombinantly produced proteins labeled via thiol-maleimide chemistry with organic fluorophores—in this case, Atto 532 in combination with three different acceptors: Biotium CF680R, Atto 647N and Abberior Star 635 (Online Methods).

We chose microinjection[2,5,14] for the targeted introduction of FRET-labeled proteins into cultured eukaryotic cells. Compared to transfection techniques such as scrape-loading[21], electroporation[22] and cell-penetrating peptides[23], microinjection offered the best control and reproducibility of the amount of protein applied; it enabled the shortest delay between protein application and measurement and is compatible with fluorescence detection directly after injection; it preserved cell adherence, which avoids problems with positional drift of the cells during measurements; and it creates the opportunity to inject molecules selectively into different cellular compartments. Microinjection enabled the reproducible introduction of sample concentrations in the picomolar to low nanomolar range, with cell viability extending far beyond the required observation times (Online Methods and **Supplementary Fig. 1**).

Measurements comprised the following iterative steps. First, we performed a reference measurement in the extracellular medium by placing the tip of the injection needle close to the confocal observation volume and ejecting several pulses of sample into free solution. Fluorescence bursts from molecules diffusing through the laser focus allowed us to confirm the integrity of the sample and functionality of the microinjection system. Analysis of these data permitted direct comparison of the conformational and dynamic properties of the labeled protein outside and inside a cell. In the next step, we injected a suitable amount of protein into a cell. The intracellular distribution of the labeled protein could then be monitored by a confocal sample scan (**Fig. 1** and **Supplementary Fig. 2**). Because we used single-photon counting in combination with pulsed excitation, fluorescence lifetime imaging microscopy[24] (FLIM) could be employed to differentiate

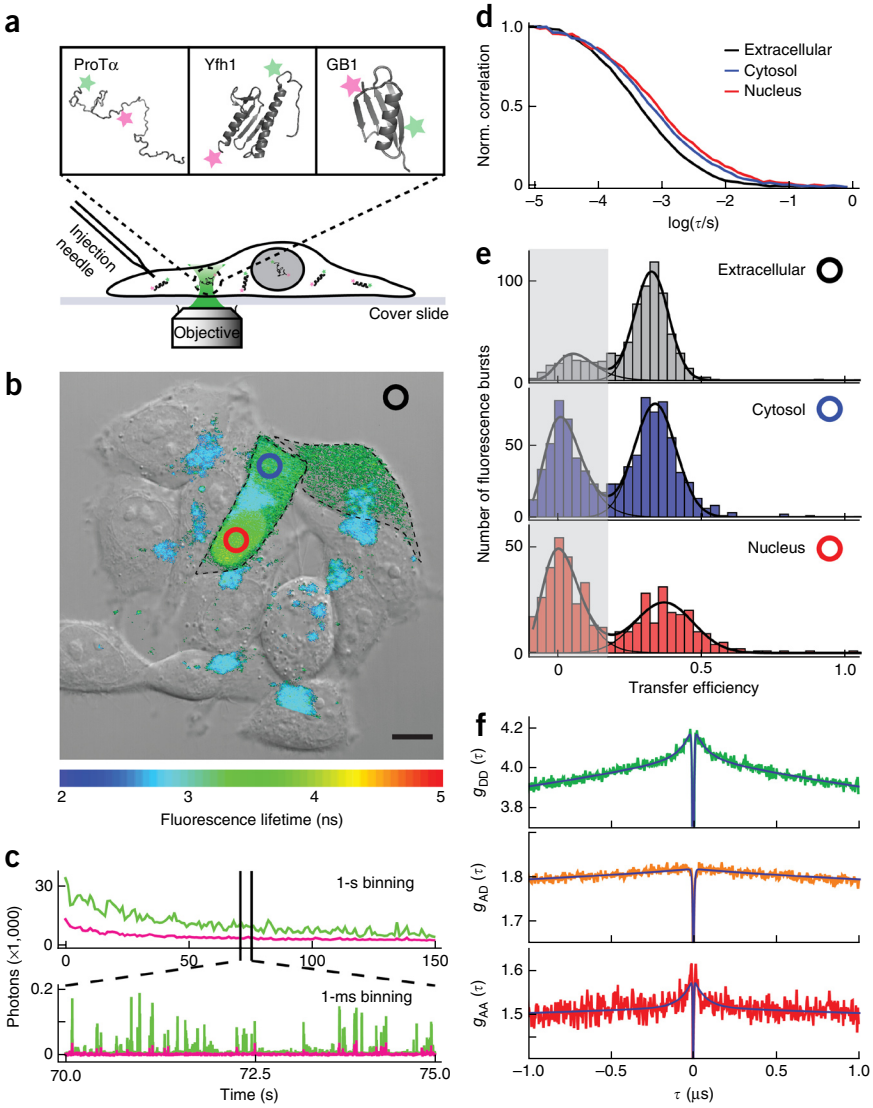

Figure 1 | Single-molecule fluorescence measurements in living cells. (**a**) Schematic of confocal single-molecule FRET studies of fluorescently labeled prothymosin α (ProTα), yeast frataxin homolog Yfh1, and IgG-binding domain of protein G (GB1) microinjected into adherent HeLa cells. (**b**) Fluorescence lifetime image (overlaid with differential interference contrast image) of HeLa cells after cytosolic injection of ProTα (injected cells indicated by dashed lines); donor fluorescence of ProTα exhibits a higher average lifetime (~3.5 ns) than the cellular autofluorescence (<3 ns). Circles indicate positions of the confocal volume in the nucleus (red), cytosol (blue) and extracellular medium (black). Scale bar, 10 μm. (**c**) Fluorescence time trace recorded in the cytosol of an injected cell. Photobleaching results in a characteristic intensity decay (1-s binning). With 1-ms binning, fluorescence bursts of donor (green) and acceptor (magenta) photons are visible. (**d**) Donor-acceptor cross-correlation curves were used to compare the translational diffusion of ProTα in buffer ($\tau_{Diff} = 0.7 \pm 0.1$ ms, $n = 5$), cytosol ($\tau_{Diff} = 1.8 \pm 0.7$ ms, $n = 33$) and nucleus ($\tau_{Diff} = 1.6 \pm 0.6$ ms, $n = 29$). (**e**) Single-cell FRET efficiency histograms of ProTα in the cytosol and nucleus show a single population at $\langle E \rangle \approx 0.35$, similar to measurements in buffer. The shaded peak at $\langle E \rangle \approx 0$ originates from molecules lacking an active acceptor chromophore (**Supplementary Fig. 5**). (**f**) nsFCS curves obtained from averaging 51 cytosolic measurements yield information about the chain reconfiguration time of ProTα on the submicrosecond timescale (g_{DD}, donor-donor correlation; g_{AD}, acceptor-donor correlation; g_{AA}, acceptor-acceptor correlation).

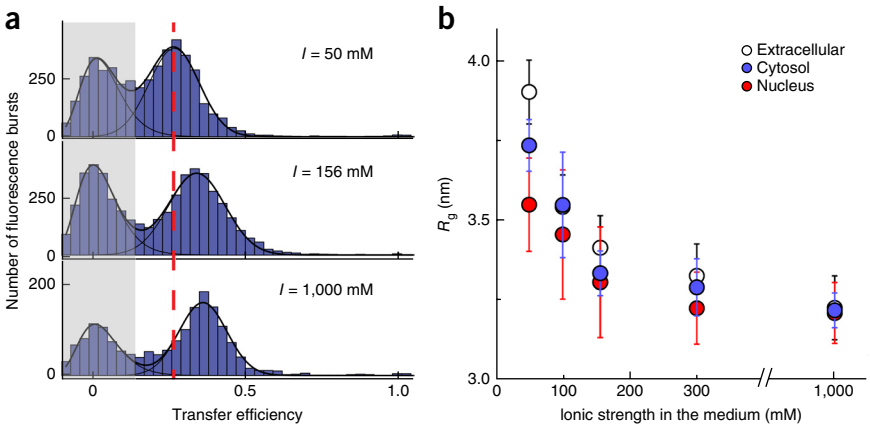

Figure 2 | Single-molecule FRET can detect small changes in protein conformation within live cells. (**a**) FRET efficiency histograms of ProTα in the cytosol of HeLa cells incubated in medium with different ionic strengths (the range of donor-only signal is shaded in gray). The red dashed line indicates the mean transfer efficiency of ProTα at I = 50 mM. (**b**) The collapse of ProTα (shown in terms of the radius of gyration, R_g, calculated from the transfer efficiencies; Online Methods) in the cytosol, nucleus and extracellular buffer. The s.d. of R_g for extracellular measurements was estimated from the variance of *in vitro* measurements performed on different instruments. The error bars for cytosolic and nuclear measurements represent the s.d. from cell-to-cell variation (Online Methods).

the emission of the injected sample from cellular autofluorescence (**Fig. 1b**), but imaging based on fluorescence intensity was adequate in most cases (**Supplementary Fig. 3**). We then acquired the actual single-molecule measurements by positioning the confocal volume at the cellular location of choice—for example, in the nucleus or the cytosol. If a fixed position was selected, predominantly freely diffusing molecules were observed; by slowly scanning across the region of interest, a defined volume could be probed (**Supplementary Fig. 4**) and potentially immobile molecules detected.

In contrast to measurements *in vitro*, the number of molecules available in microinjected cells is limited by the small cell volume. Measurements at the ~20–100 pM concentrations required for the confocal observation of single molecules were thus restricted to a few minutes before all molecules were photobleached. However, this time was sufficient for obtaining transfer efficiency histograms from single-cell measurements and, thus, assessing potential cell-to-cell variation of protein conformation (**Fig. 1e**). Compared to camera-based imaging approaches, whose strength is the parallel tracking of many molecules on longer timescales, confocal single-molecule detection provides additional observables from spectrally and polarization-selective single-photon counting[16], including fluorescence lifetimes (**Fig. 1b** and **Supplementary Fig. 5**), anisotropies (**Supplementary Fig. 6**) and, most importantly, dynamics in the millisecond range and even below[6,17,25–27].

Protein diffusivity, structure and conformational dynamics

We first tested the approach with confocal single-molecule measurements of the IDP[28,29] prothymosin α (ProTα)[28,30] in live cells. ProTα is a highly negatively charged protein that does not assume a folded structure under any known conditions and whose intramolecular distance distributions and dynamics have previously been characterized by single-molecule experiments *in vitro*[31–33]. First, fluorescence imaging after microinjection of ProTα labeled with Atto 532 and Biotium CF680R was used to monitor the intracellular distribution of the labeled protein (**Supplementary Fig. 2**). We quantified translational diffusion by correlating the fluorescence signal from the confocal measurements[6,26]. As expected, the intracellular diffusion time of ProTα increased relative to the diffusion time of the extracellular medium (**Fig. 1d**; to a similar extent in cytoplasm and nucleus), corresponding to an effective intracellular viscosity of 2.8 ± 1.1 mPa s (±s.d. from cell-to-cell variability unless otherwise specified; n = 39), which is within the range previously reported[34].

To quantify the dimensions of the protein, we used the distance dependence of intramolecular FRET. From measurements in individual cells, we obtained ~200–800 fluorescence bursts within the observation time of ~3 min before the majority of injected molecules were photobleached. We measured FRET efficiency histograms of ProTα with extracellular, cytosolic and nuclear localization (**Fig. 1e**). In all cases, a single population of FRET-labeled ProTα molecules with similar mean transfer efficiencies, $\langle E \rangle$, was observed. The cell-to-cell variation of $\langle E \rangle$ (s.d. = 0.02) was only slightly greater than its uncertainty from photon statistics (0.01) and close to the difference between cytosolic ($\langle E \rangle = 0.34 \pm 0.01$, $n = 8$) and nuclear measurements ($\langle E \rangle = 0.35 \pm 0.03$, n = 8). If we use a simple Gaussian chain model[32] to estimate the radius of gyration, R_g, of intracellular ProTα, we obtain 3.3 ± 0.1 nm (n = 8) in the cytosol and 3.3 ± 0.2 nm (n = 8) in the nucleus, very similar to the value in the extracellular medium (3.4 ± 0.1 nm, error propagated from the s.d. of $\langle E \rangle$) and to previous results *in vitro*[32]. The presence of an immobile subpopulation with different conformational properties was excluded by scanning over the intracellular region of interest during data acquisition (**Supplementary Fig. 4**).

For ProTα, as for other IDPs, nanosecond FCS (nsFCS) has been used to identify the characteristic chain-reconfiguration times on the 10- to 100-ns timescale[17,31]. We injected labeled ProTα and averaged the recordings from 51 cells with a total acquisition time of 2.5 h. The resulting submicrosecond correlation functions were of sufficient quality for us to discern the main features identified in previous *in vitro* measurements[17,25] (**Fig. 1f**): the drop of the correlation in the low nanosecond range owing to photon antibunching characteristic of single-molecule detection, as well as photon bunching with a slower decay and a time constant of 62 ± 6 ns (s.d. from splitting the data into three equal parts) originating from the intramolecular distance fluctuations in the IDP. These dynamics, which were slightly slower than those measured *in vitro* (24 ± 4 ns, n = 3 (15-h measurement each)), were in good agreement with the increased intracellular viscosity identified by translational diffusion measurements (**Fig. 1**). The presence of a broad and rapidly reconfiguring ensemble of conformations is further supported by the dependence of fluorescence lifetimes on transfer efficiency (**Supplementary Fig. 5**).

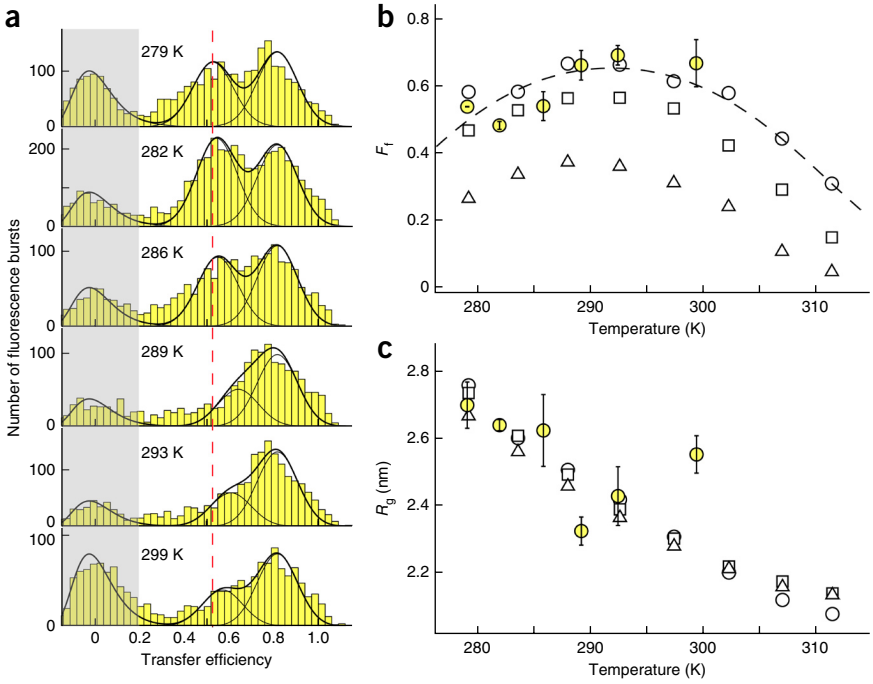

Figure 3 | Temperature dependence of protein stability and cold denaturation measured in live HeLa cells. (**a**) Single-molecule FRET efficiency histograms of Yfh1 microinjected into HeLa cells at different temperatures. The peak at $\langle E \rangle \approx 0.82$ corresponds to folded Yfh1; the peak at lower transfer efficiencies corresponds to unfolded Yfh1. For details on the fitting procedure, see Online Methods. (**b**) The fraction of folded Yfh1 (F_f) shows the temperature dependence of the intracellular conformational stability of Yfh1 (yellow circles), calculated as the ratio of the peak area of the folded state and the sum of the peak areas of folded and unfolded states (**a**). For comparison, the results of *in vitro* experiments in HBSS (white circles), HBSS without Ca^{2+} and Mg^{2+} (squares) and sodium phosphate, pH 7.0, (triangles) are shown. The intracellular temperature dependence of F_f was fitted assuming a constant heat capacity change of unfolding (dashed line), as previously described[40]. (**c**) The temperature dependence of the radius of gyration (R_g; Online Methods) of unfolded Yfh1 inside HeLa cells (yellow circles) and in buffer (HBSS, white circles; HBSS without Ca^{2+} and Mg^{2+}, squares; sodium phosphate, pH 7.0, triangles). The data points of the in-cell measurements in **b**,**c** were obtained from the global fit shown in **a**. Error bars correspond to s.d. estimated by splitting each data set into two and treating F_f or R_g of the unfolded population determined from each half as independent measurements.

The notable similarity of the intra- and extracellular behavior of ProTα may raise the question of whether in-cell single-molecule FRET experiments are sensitive enough to detect small changes in conformation. The intramolecular distance distributions of the highly negatively charged ProTα have previously been shown to be very responsive to charge screening with changes in ionic strength[32,33]. We mimicked this situation by increasing the extracellular salt concentration, which is expected to lead to a transient increase in intracellular ionic strength[35]. Indeed, the resulting decrease in the R_g of intracellular ProTα as derived from the transfer efficiencies showed a similar trend to the extracellular behavior (**Fig. 2**), indicating that even small changes in intramolecular distances of 0.2–0.3 nm were detectable in cells.

Temperature-dependent intracellular protein stability

Detecting changes in conformational stability *in vivo* is another important aspect for identifying the effect of cellular factors on biomolecular behavior[3,36,37]. We investigated the effect of temperature on the conformational properties of the yeast homolog of frataxin (Yfh1)[38–40]. Frataxin exhibits cold denaturation in a readily accessible temperature range, i.e., it unfolds not only at high temperature but also below ~290 K. We labeled the protein with Atto 532 and Abberior Star 635 and developed a temperature-controlled stage optimized for cell culture observation and microinjection combined with single-molecule detection (**Supplementary Fig. 7**).

Transfer efficiency histograms of labeled frataxin after its injection into live cells at different temperatures showed two populations with a folded state at $\langle E \rangle \approx 0.82$ and an unfolded state at lower transfer efficiency (**Fig. 3**). In spite of the lower signal-to-noise ratio, the data reflected the behavior observed *in vitro*[40] (**Supplementary Fig. 8**). By extracting the fraction of folded protein from the peak areas, we detected a maximum in conformational stability of the protein at ~290 K and a decrease at both lower and higher temperatures, corresponding to cold and heat denaturation. The behavior was very sensitive to buffer conditions, especially to salt concentrations[39] (**Fig. 3b**). In HBSS buffer, the stability was at the same level as in cells, pointing toward good consistency of this optimized cell culture medium with the cellular ion concentrations. Measurements in HBSS buffer without Ca^{2+} and Mg^{2+} confirmed the pronounced sensitivity of frataxin stability to divalent ions[39]. The intracellular single-molecule measurements of frataxin were consistent with the compaction of its unfolded state with increasing temperature previously observed in buffer[40] (**Fig. 3c**).

Single-molecule protein-folding kinetics in the cell

Single-molecule spectroscopy enables kinetics to be extracted from equilibrium measurements, a quality that is particularly valuable in the cell, where the choice of perturbations compatible with cellular homeostasis is very limited. As a model for metastable cellular proteins that exhibit equilibrium conformational interconversion dynamics, we investigated a variant of GB1, the IgG-binding domain of protein G labeled with Atto 532 and Atto 647N. Its conformational stability and folding kinetics in the millisecond range have been well characterized *in vitro*[41] and *in vivo*[42]. By using a slightly destabilized variant (Online Methods), we could populate both folded and unfolded states at equilibrium under physiological conditions, as reflected by the two peaks in the transfer efficiency histogram at $\langle E \rangle = 1.00$ and 0.85, respectively (**Fig. 4** and **Supplementary Fig. 9**).

To extract the rate of interconversion between the folded and unfolded conformations at equilibrium, we used recurrence analysis of single particles (RASP), an approach that has recently

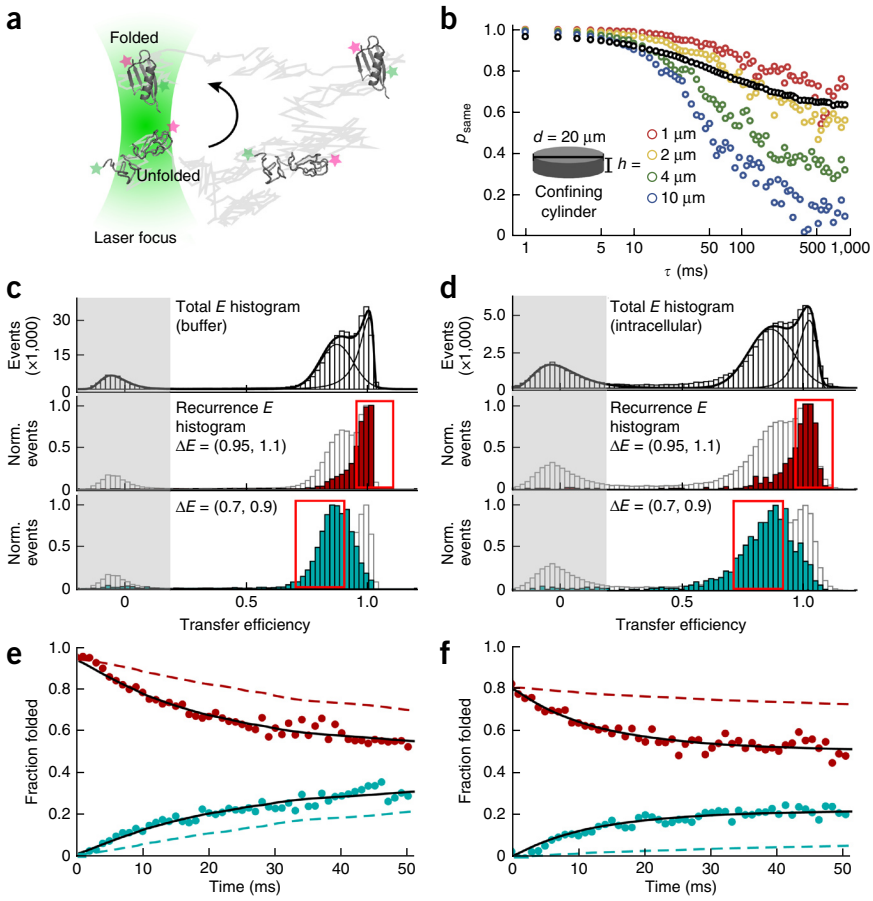

Figure 4 | Intracellular protein-folding dynamics from recurrence analysis (RASP)[43]. (**a**) Schematic of a protein recurring to the confocal volume; in this example, the protein happens to fold between detected fluorescence bursts. (**b**) Comparison of the experimental p_{same} curve obtained in cells (black) with simulated p_{same} curves of proteins in a confining cylinder (diameter, 20 μm; height, 1–10 μm; protein concentration, 100 pM). (**c**,**d**) FRET efficiency histograms of GB1 in 50 mM phosphate buffer (**c**) and inside cells (**d**). The range of donor-only signal is shaded in gray, and the initial transfer efficiency range, ΔE, is indicated with red boxes. Recurrence FRET efficiency histograms show the folded (red, ΔE = (0.95–1.1)) and unfolded (cyan, ΔE = (0.7–0.9)) populations of GB1 within a recurrence interval T = (0, 1 ms) (measurements performed at 4 °C; Online Methods). (**e**,**f**) Fractions of folded molecules from recurrence FRET efficiency histograms with increasing recurrence intervals (**Supplementary Fig. 10**) starting from unfolded (cyan) and folded molecules (red). Global fits (solid lines) yielded relaxation times of 21 ± 4 ms (buffer, **e**) and 12 ± 2 ms (intracellular, **f**). Dashed lines show the behavior expected in the absence of folding dynamics (i.e., from the appearance of new molecules only), as calculated from burst time correlation analysis[43]. Differences between dashed and solid lines indicate population interconversion on the millisecond timescale (for a control measurement with noninterconverting species, see **Supplementary Fig. 11**).

been shown *in vitro* to allow quantification of conformational changes on timescales from ~50 μs to ~100 ms (ref. 43; **Fig. 4**, Online Methods and **Supplementary Fig. 10**). Cellular confinement strongly increases the same-molecule probability, $p_{same}(\tau)$, i.e., the probability that two fluorescence bursts separated by time τ are emitted by the same molecule, as illustrated by simulations in a cylindrical volume (**Fig. 4b**). For cylinder heights of 1–2 μm (dimensions similar to those of an adherent HeLa cell), the p_{same} decays closely resemble intracellular measurements, with p_{same} values of around 60% for timescales of seconds. This effect extends the effective observation time and makes recurrence analysis ideally suited for probing intracellular conformational dynamics.

RASP yielded a relaxation time for GB1 folding-unfolding of 21 ± 4 ms in buffer (error from the fit, valid for all decay times shown here; equilibrium constant K_{eq} = 1.3 ± 0.1), in agreement with the time of 23 ± 7 ms (K_{eq} = 1.5 ± 0.1) obtained from single-molecule perturbation experiments using microfluidic mixing under the same solution conditions (Online Methods and **Supplementary Fig. 9**) and in the range expected from previous work[41]. In HeLa cells, the transfer efficiency histogram of the microinjected GB1 variant was broadened compared to buffer measurements—for example, from the additional background contribution; nevertheless, two populations could be identified, as further supported by the recurrence FRET efficiency histograms, which allow the peaks from folded and unfolded protein to be clearly separated[43] (**Fig. 4** and **Supplementary Fig. 10**). We observed, on the basis of the peak integrals, a similar fraction of folded state (0.33 ± 0.03) to that in buffer (0.43 ± 0.02). RASP analysis of the intracellular measurements yielded a folding-unfolding relaxation time of 12 ± 2 ms (K_{eq} = 2.0 ± 0.2; **Fig. 4**), indicating at most a small effect of the cellular environment—such as from macromolecular crowding—on the conformational stability and folding dynamics of GB1 (refs. 37,44). We demonstrated the robustness of the RASP method by performing control measurements with noninterconverting species in buffer and injected into cells (**Supplementary Fig. 11**).

DISCUSSION

The results presented here show that an integrated approach addressing the multifactorial challenges of in-cell single-molecule spectroscopy enables the application of a broad spectrum of confocal single-molecule fluorescence methods in eukaryotic cells. With single-molecule FRET and the resulting separation of subpopulations, not only can intramolecular distances be quantified, but the conformational stability of proteins can be measured in live cells and compared to *in vitro* observations (**Figs. 3** and **4**), including the effects of temperature. The dimensions of intrinsically disordered and unfolded proteins are accessible (**Figs. 1–3**), as are their responses to changes in intracellular conditions, such as ion concentrations and temperature (**Figs. 2** and **3**). Most notably, the approach enables in-cell conformational dynamics to be investigated, illustrated here by the use of nsFCS for quantifying submicrosecond reconfiguration times (**Fig. 1**) and the analysis of FRET efficiency histograms with recurrence analysis to extract millisecond protein-folding kinetics (**Fig. 4**). Together with the well-known possibility of determining

intracellular diffusivity with FCS[6,26], the effective intracellular viscosity can be monitored from molecular to cellular length scales. All of these observables are accessible as a function of cellular localization (**Fig. 1**) and thus enable the investigation of spatial variations in conformation and dynamics. The availability of FLIM can aid the discrimination between the signal of the injected sample and autofluorescence (**Fig. 1**).

Our observations exemplify how this methodology can provide new possibilities for probing the properties of biomolecules in live cells. The single-molecule FRET experiments on ProTα clearly showed that this IDP remains unstructured in the cell, as judged from its dimensions and submicrosecond chain dynamics (**Fig. 1**). Similar conclusions were previously drawn for α-synuclein via intracellular NMR-based experiments[45,46], indicating that even though many IDPs are known to form a folded structure upon interaction with their cellular targets[29], IDPs can stay unfolded upon binding and in live cells. The results on protein GB1 and frataxin indicated a remarkable robustness in the conformational stabilities and even folding kinetics of these proteins in cells compared to in simple buffered solutions (**Figs. 3** and **4**). However, even modest changes in quantitative behavior may have important functional or regulatory consequences[2,36]. The sensitivity of the in-cell single-molecule approach (**Figs. 2** and **3**) is thus expected to be ideally suited for studying the effects of molecular crowding[44] and the cellular machinery on the conformations, dynamics and intracellular interactions of biological macromolecules, even as a function of cellular localization.

Our approach complements existing single-molecule methods in eukaryotes[14] and prokaryotes[10–13] and other techniques. In-cell NMR spectroscopy, for example, can provide atomistic detail and a wide range of dynamics[37,42,45,47], but it is currently limited to averages over large molecular ensembles and many cells. Recent advances in quantitative cellular FRET imaging based on fusions with fluorescent proteins and temperature jumps have led to the spatiotemporal mapping of protein stability and kinetics with high sensitivity[3,36], but this ensemble technique requires rapid changes in temperature as a perturbation and is currently limited to timescales in the seconds range and above. Finally, super-resolution microscopy[8,9] now routinely enables fluorescence imaging with spatial resolution of tens of nanometers, but conformational changes and dynamics at the time and length scales investigated here have remained beyond its reach. We therefore expect that single-molecule spectroscopy will play an important role in bridging the gap between our quantitative understanding of biomolecules *in vitro* and *in vivo*.

METHODS

Methods and any associated references are available in the online version of the paper.

Note: Any Supplementary Information and Source Data files are available in the online version of the paper.

ACKNOWLEDGMENTS

We thank S. Weidner and A. Schmid for excellent technical assistance in instrumentation development, A. Holla and H. Hofmann for discussions regarding the choice of fluorophores, A. Flütsch (University of Zurich) for providing HeLa cells, and K. Buholzer for assistance with culturing cells. B.S. was supported by the Swiss National Science Foundation and the European Research Council. A.Z.-A. was supported by the Human Frontier Science Program. M.A. was supported by a Postdoctoral Fellowship from the Forschungskredit of the University of Zurich (FK-13-034). J.C.S. was supported by a Chemiefonds fellowship of the German Chemical Industry Fund. Differential interference contrast imaging was performed at the Center for Microscopy and Image Analysis, University of Zurich.

AUTHOR CONTRIBUTIONS

B.S. designed the project together with I.K., A.Z.-A. and M.A.; I.K., A.Z.-A. and M.A. performed the experiments; I.K., A.Z.-A., M.A., A.S. and D.N. analyzed the data; J.C.S. and I.K. conducted cell culture experiments; A.Z.-A., B.W. and F.D. performed and analyzed microfluidics experiments; I.K., M.A., B.W. and D.N. developed instrumentation; A.P., A.S., D.N. and B.S. supervised the project; I.K., A.Z.-A., M.A., D.N. and B.S. wrote the paper with the help of all authors.

COMPETING FINANCIAL INTERESTS

The authors declare no competing financial interests.

1. Shaner, N.C., Steinbach, P.A. & Tsien, R.Y. A guide to choosing fluorescent proteins. *Nat. Methods* **2**, 905–909 (2005).
2. Phillip, Y., Kiss, V. & Schreiber, G. Protein-binding dynamics imaged in a living cell. *Proc. Natl. Acad. Sci. USA* **109**, 1461–1466 (2012).
3. Ebbinghaus, S., Dhar, A., McDonald, J.D. & Gruebele, M. Protein folding stability and dynamics imaged in a living cell. *Nat. Methods* **7**, 319–323 (2010).
4. Fenz, S.F., Pezzarossa, A. & Schmidt, T. in *Comprehensive Biophysics* Vol. 2 (ed. Egelman, E.H.) Ch. 13, 260–272 (Elsevier, 2012).
5. Pitchiaya, S., Heinicke, L.A., Custer, T.C. & Walter, N.G. Single molecule fluorescence approaches shed light on intracellular RNAs. *Chem. Rev.* **114**, 3224–3265 (2014).
6. Mütze, J., Ohrt, T. & Schwille, P. Fluorescence correlation spectroscopy *in vivo*. *Laser Photon. Rev.* **5**, 52–67 (2011).
7. Digman, M.A. & Gratton, E. Scanning image correlation spectroscopy. *Bioessays* **34**, 377–385 (2012).
8. Hell, S.W. Far-field optical nanoscopy. *Science* **316**, 1153–1158 (2007).
9. Jones, S.A., Shim, S.H., He, J. & Zhuang, X. Fast, three-dimensional super-resolution imaging of live cells. *Nat. Methods* **8**, 499–508 (2011).
10. Persson, F., Barkefors, I. & Elf, J. Single molecule methods with applications in living cells. *Curr. Opin. Biotechnol.* **24**, 737–744 (2013).
11. Stratmann, S.A. & van Oijen, A.M. DNA replication at the single-molecule level. *Chem. Soc. Rev.* **43**, 1201–1220 (2014).
12. Uphoff, S., Reyes-Lamothe, R., Garza de Leon, F., Sherratt, D.J. & Kapanidis, A.N. Single-molecule DNA repair in live bacteria. *Proc. Natl. Acad. Sci. USA* **110**, 8063–8068 (2013).
13. Crawford, R. *et al.* Long-lived intracellular single-molecule fluorescence using electroporated molecules. *Biophys. J.* **105**, 2439–2450 (2013).
14. Sakon, J.J. & Weninger, K.R. Detecting the conformation of individual proteins in live cells. *Nat. Methods* **7**, 203–205 (2010).
15. Selvin, P.R. & Ha, T. *Single-Molecule Techniques: A Laboratory Manual* (Cold Spring Harbor Laboratory Press, 2008).
16. Sisamakis, E., Valeri, A., Kalinin, S., Rothwell, P.J. & Seidel, C.A.M. Accurate single-molecule FRET studies using multiparameter fluorescence detection. *Methods Enzymol.* **475**, 455–514 (2010).
17. Schuler, B. & Hofmann, H. Single-molecule spectroscopy of protein folding dynamics—expanding scope and timescales. *Curr. Opin. Biotechnol.* **23**, 36–47 (2013).
18. Banerjee, P.R. & Deniz, A.A. Shedding light on protein folding landscapes by single-molecule fluorescence. *Chem. Soc. Rev.* **43**, 1172–1188 (2014).
19. Verdurmen, W.P.R., Luginbühl, M., Honegger, A. & Plückthun, A. Efficient cell-specific uptake of binding proteins into the cytoplasm through engineered modular transport systems. *J. Control. Release* **200**, 13–22 (2015).
20. Aubin, J.E. Autofluorescence of viable cultured mammalian cells. *J. Histochem. Cytochem.* **27**, 36–43 (1979).
21. McNeil, P.L., Murphy, R.F., Lanni, F. & Taylor, D.L. A method for incorporating macromolecules into adherent cells. *J. Cell Biol.* **98**, 1556–1564 (1984).
22. Morgan, W.F. & Day, J.P. The introduction of proteins into mammalian cells by electroporation. *Methods Mol. Biol.* **48**, 63–71 (1995).
23. Milletti, F. Cell-penetrating peptides: classes, origin, and current landscape. *Drug Discov. Today* **17**, 850–860 (2012).
24. Berezin, M.Y. & Achilefu, S. Fluorescence lifetime measurements and biological imaging. *Chem. Rev.* **110**, 2641–2684 (2010).

25. Nettels, D., Gopich, I.V., Hoffmann, A. & Schuler, B. Ultrafast dynamics of protein collapse from single-molecule photon statistics. *Proc. Natl. Acad. Sci. USA* **104**, 2655–2660 (2007).
26. Rigler, R. & Elson, E.S. *Fluorescence Correlation Spectroscopy: Theory and Applications* (Springer, 2001).
27. Gopich, I.V. & Szabo, A. in *Single-Molecule Biophysics: Experiment and Theory* Vol. 146 (eds. Komatsuzaki, T., Kawakami, M., Takahashi, S., Yang, H. & Silbey, R.J.) 245–297 (Wiley, 2011).
28. Uversky, V.N. What does it mean to be natively unfolded? *Eur. J. Biochem.* **269**, 2–12 (2002).
29. Wright, P.E. & Dyson, H.J. Linking folding and binding. *Curr. Opin. Struct. Biol.* **19**, 31–38 (2009).
30. Gast, K. *et al.* Prothymosin alpha: a biologically active protein with random coil conformation. *Biochemistry* **34**, 13211–13218 (1995).
31. Soranno, A. *et al.* Quantifying internal friction in unfolded and intrinsically disordered proteins with single molecule spectroscopy. *Proc. Natl. Acad. Sci. USA* **109**, 17800–17806 (2012).
32. Müller-Späth, S. *et al.* Charge interactions can dominate the dimensions of intrinsically disordered proteins. *Proc. Natl. Acad. Sci. USA* **107**, 14609–14614 (2010).
33. Soranno, A. *et al.* Single-molecule spectroscopy reveals polymer effects of disordered proteins in crowded environments. *Proc. Natl. Acad. Sci. USA* **111**, 4874–4879 (2014).
34. Kalwarczyk, T. *et al.* Comparative analysis of viscosity of complex liquids and cytoplasm of mammalian cells at the nanoscale. *Nano Lett.* **11**, 2157–2163 (2011).
35. Burg, M.B., Ferraris, J.D. & Dmitrieva, N.I. Cellular response to hyperosmotic stresses. *Physiol. Rev.* **87**, 1441–1474 (2007).
36. Guo, M., Xu, Y. & Gruebele, M. Temperature dependence of protein folding kinetics in living cells. *Proc. Natl. Acad. Sci. USA* **109**, 17863–17867 (2012).
37. Smith, A.E., Zhang, Z., Pielak, G.J. & Li, C. NMR studies of protein folding and binding in cells and cell-like environments. *Curr. Opin. Struct. Biol.* **30**, 7–16 (2015).
38. Pastore, A. *et al.* Unbiased cold denaturation: low- and high-temperature unfolding of yeast frataxin under physiological conditions. *J. Am. Chem. Soc.* **129**, 5374–5375 (2007).
39. Sanfelice, D. *et al.* Yeast frataxin is stabilized by low salt concentrations: cold denaturation disentangles ionic strength effects from specific interactions. *PLoS ONE* **9**, e95801 (2014).
40. Aznauryan, M., Nettels, D., Holla, A., Hofmann, H. & Schuler, B. Single-molecule spectroscopy of cold denaturation and the temperature-induced collapse of unfolded proteins. *J. Am. Chem. Soc.* **135**, 14040–14043 (2013).
41. Kuszewski, J., Clore, G.M. & Gronenborn, A.M. Fast folding of a prototypic polypeptide: the immunoglobulin binding domain of streptococcal protein G. *Protein Sci.* **3**, 1945–1952 (1994).
42. Selenko, P., Serber, Z., Gadea, B., Ruderman, J. & Wagner, G. Quantitative NMR analysis of the protein G B1 domain in *Xenopus laevis* egg extracts and intact oocytes. *Proc. Natl. Acad. Sci. USA* **103**, 11904–11909 (2006).
43. Hoffmann, A. *et al.* Quantifying heterogeneity and conformational dynamics from single molecule FRET of diffusing molecules: recurrence analysis of single particles (RASP). *Phys. Chem. Chem. Phys.* **13**, 1857–1871 (2011).
44. Zhou, H.-X., Rivas, G. & Minton, A.P. Macromolecular crowding and confinement: biochemical, biophysical, and potential physiological consequences. *Annu. Rev. Biophys.* **37**, 375–397 (2008).
45. Binolfi, A., Theillet, F.X. & Selenko, P. Bacterial in-cell NMR of human α-synuclein: a disordered monomer by nature? *Biochem. Soc. Trans.* **40**, 950–954 (2012).
46. Waudby, C.A. *et al.* In-cell NMR characterization of the secondary structure populations of a disordered conformation of α-synuclein within *E. coli* cells. *PLoS ONE* **8**, e72286 (2013).
47. Tochio, H. Watching protein structure at work in living cells using NMR spectroscopy. *Curr. Opin. Chem. Biol.* **16**, 609–613 (2012).

ONLINE METHODS

Protein expression and labeling. Fluorescent dyes for single-molecule experiments were chosen according to their availability as a maleimide derivative for site-specific labeling and their photophysical (photostability and brightness) and chemical (hydrophobicity) properties. For probing conformational dynamics on the length and time scales required here, genetically introduced fusions with fluorescent proteins are of limited use owing to their relatively large size, lower brightness, and photostability[48]; the complication of heterogeneous expression levels[49]; and the tendency of forming oligomers[50]. We thus chose to work with organic fluorophores. The broad availability of fluorophores with absorption maxima in the vicinity of the popular 532-nm laser line facilitates the choice of a FRET donor and a corresponding acceptor dye. As a donor dye, we used Atto 532 maleimide (ATTO-TEC GmbH). For acceptor dyes, we covered a range from hydrophilic to hydrophobic dyes, specifically Biotium CF680R maleimide (Biotium Inc.), Abberior Star 635 maleimide (Abberior GmbH) and Atto 647N maleimide (ATTO-TEC GmbH). The Förster radii for the dye-pairs were calculated to be 5.7 nm for Atto 532/Biotium CF680R, 6.0 nm for Atto 532/Abberior Star 635, and 6.0 nm for Atto 532/Atto 647N on the basis of the quantum yields and absorption and emission spectra provided by the manufacturer and using an averaged orientation factor of $\kappa^2 = 2/3$, as supported by single-molecule anisotropy measurements *in vitro* and *in vivo* (**Supplementary Fig. 6** and Online Methods section "Data analysis").

The three different acceptor fluorophores (Atto 647N, Abberior Star 635 and Biotium CF680R), in combination with the donor dye Atto 532, were used to assess the robustness of different FRET pairs for measurements *in vitro* and *in vivo*. The selected acceptor dyes have absorption maxima between 634 and 680 nm and emission maxima between 654 and 701 nm (as specified by the manufacturer), in a suitable range to act as acceptors for FRET from Atto 532. Atto 647N is particularly popular for experiments both *in vitro* and *in vivo* owing to its very high photostability and brightness[51]. Abberior Star 635 was recently developed for demanding applications such as stimulated emission depletion microscopy[52]. Biotium CF680R was chosen on the basis of a screen we performed for dyes with suitably high photostability and brightness combined with low hydrophobicity; we are not aware of any previous use in single-molecule spectroscopy. A major difference between the dyes is their hydrophobicity, with Biotium CF680R being the most hydrophilic, Abberior Star 635 being moderately hydrophobic, and Atto 647N exhibiting the highest hydrophobicity according to the elution times in reversed-phase HPLC. Our results showed that the FRET pairs Atto 532/Biotium CF680R on ProTα (**Figs. 1** and **2**), Atto532/Abberior Star 635 on frataxin (**Fig. 3**) and Atto 532/Atto 647N on GB1 (**Fig. 4**) are all suitable for in-cell single-molecule spectroscopy, indicating that the method is not limited to specific fluorophores. However, care has to be taken regarding the hydrophobicity of the dyes. Especially Atto647N is known for its hydrophobicity[53], which can lead to nonspecific interactions with other molecules or even the labeled protein itself. It is therefore essential to characterize labeled proteins *in vitro* before using them in *in vivo* experiments: for example, regarding the conformational stability (**Fig. 3**), the fluorescence lifetime of the attached dyes (**Supplementary Fig. 5**), or fluorescence anisotropy (**Supplementary Fig. 6**). In the cases of ProTα, Frataxin and GB1, no interfering interactions were observed after we labeled them with the dye pairs used here.

Prothymosin α (ProTα). Cysteine residues for the specific labeling of ProTα using maleimide chemistry were introduced by site-directed mutagenesis at the positions 1 and 56 (**Supplementary Table 1**). ProTα was produced in *Escherichia coli* BL21 with an N-terminal His-tag for purification. Cells were grown in LB medium, expression was induced with isopropyl β-D-1-thiogalactopyranoside (IPTG, Sigma), and the harvested cells were disrupted. As previously described[33], ProTα was purified with a Ni-NTA column (Thermo Scientific) after ammonium sulfate precipitation[54]. The His-tag was cleaved off with HRV 3C protease (recombinantly produced in-house as a hexahistidine fusion), followed by a second Ni-NTA chromatography run to remove the His-tag and the protease. ProTα was reduced with 10 mM tris(2-carboxyethyl) phosphine (TCEP, Sigma) and further purified by reversed-phase high-pressure liquid chromatography (RP-HPLC) on a Reprosil Gold 200 column (Dr. Maisch GmbH) with an acetonitrile gradient. Purified ProTα was lyophilized in a SpeedVac concentrator (Thermo Scientific), dissolved in 0.1 M sodium phosphate (Sigma) buffer, pH 7.2, and labeled with Atto 532 maleimide according to the supplier's manual at a molar ratio of dye to protein of 0.8:1. The reaction was stopped with β-mercaptoethanol (Sigma), reduced with 10 mM TCEP and purified by RP-HPLC on an XTerra C18 column (Waters), which enabled not only the separation of singly labeled, doubly labeled and unlabeled protein but also the separation of the singly labeled permutants, as confirmed by proteolytic digest and electrospray ionization mass spectrometry (ESI-MS). The fraction containing one of the singly labeled ProTα permutants was lyophilized in a SpeedVac concentrator and was labeled and purified analogously with a molar excess of Biotium CF680R maleimide. The mass of the doubly labeled ProTα was confirmed by ESI-MS.

Yeast frataxin homolog Yfh1. The expression and purification of Yfh1 (**Supplementary Table 1**) was performed as previously described[40]. Purified Yfh1 was first labeled with Atto 532 maleimide in 6 M guanidinium chloride (GdmCl), 100 mM sodium phosphate, pH 7.1, at a molar ratio of dye to protein of 0.7:1 for 2 h at room temperature. Singly labeled Yfh1 was isolated from the reaction mixture by RP-HPLC using a Reprosil Gold C18 column with a water-acetonitrile gradient, which enabled not only the separation of singly labeled, doubly labeled and unlabeled protein but also the separation of the singly labeled permutants. The lyophilized fractions containing one of the singly labeled permutants of Yfh1 were further labeled with Abberior Star 635 maleimide. A twofold molar excess of Abberior Star 635 was reacted with singly Atto 532–labeled protein in 6 M GdmCl, 100 mM sodium phosphate, pH 7.1, for 2 h at room temperature. The purification of the doubly labeled Yfh1 was again performed by RP-HPLC, as described above. The mass of doubly labeled Yfh1 was confirmed by ESI-MS.

IgG-binding domain of protein G (GB1). A variant of GB1 (ref. 55) containing the destabilizing F30L-G41A substitutions[56] (**Supplementary Table 1**) was site-specifically labeled at positions Q2C and T55C (very close to the termini to achieve the lowest possible transfer efficiency compared to the folded state) with the maleimide derivatives of the donor Atto 532 and the acceptor Atto 647N, respectively. GB1 was expressed with an N-terminal His-tag followed by a cleavage site for tobacco etch

doi:10.1038/nmeth.3475

virus (TEV) protease using *E. coli* Rosetta DE3 cells (Millipore). The cells were cotransfected with the pRARE plasmid (Millipore) to further boost the expression of GB1. The Rosetta cells were grown in 2YT medium, and expression was induced with IPTG. The harvested cells were lysed in 6 M GdmCl (Sigma), 100 mM sodium phosphate, 10 mM Tris-HCl (Sigma), 10 mM imidazole (Sigma), pH 8.0 (binding buffer), by rocking them at room temperature for 1 h. Insoluble proteins and cellular debris were then pelleted, and the supernatant was incubated with 5 ml Ni-NTA agarose slurry (Thermo Scientific). The slurry was gently pelleted and washed with binding buffer four times. Bound GB1 was eluted by incubating the slurry in 6 M GdmCl, 0.2 M acetic acid (Sigma), pH 4.5, for 20 min, rocking at room temperature. The supernatant containing GB1 was filtered through a 0.45-μm filter (TPP) and refolded by equilibrium dialysis (3-kDa-cutoff membrane, Spectrum Laboratories) against three times 4 liters of 50 mM sodium phosphate, 300 mM sodium chloride (Sigma), pH 7.0, at 4 °C. TEV protease (recombinantly produced in-house as a hexahistidine fusion) was added to GB1 at a molar ratio of 50:1 (GB1/TEV) along with 5 mM dithiothreitol (Sigma) to cleave off the His-tag, followed by dialysis against 50 mM sodium phosphate, 300 mM NaCl, pH 8.0, as above. GB1 was then subjected to a second round of Ni-NTA pulldown (equilibrated in the same buffer) to remove the cleaved His-tag as well as the TEV protease. GB1 was further purified with size-exclusion chromatography on a Superdex 75 column (GE Healthcare) in 50 mM potassium phosphate, 100 mM NaCl, 0.5 mM EDTA (Sigma), at pH 7.5. Fractions containing GB1 were collected and were subjected to RP-HPLC on a Reprosil Gold C18 column to remove additional degradation products. Protein samples were reduced with TCEP and eluted with an acetonitrile gradient. Samples were subsequently lyophilized and labeled with Atto 532 maleimide at a molar ratio of dye to protein of 0.7:1. The reaction products were purified by RP-HPLC using an acetonitrile gradient on an XTerra C18 column, which enabled not only the separation of singly labeled, doubly labeled and unlabeled protein but also the separation of the singly labeled permutants. The purified protein fraction containing one of the singly labeled permutants was subsequently lyophilized and labeled with Atto 647N maleimide with a molar ratio of protein to dye of 1:3. The reaction mixture was purified by reversed-phase HPLC using an acetonitrile gradient on an XTerra C18 column, as above. The mass of doubly labeled GB1 was confirmed by ESI-MS. Yields of correctly FRET-labeled samples were >90% for all three proteins, as indicated by HPLC elution profiles, mass spectrometry, and the low 'donor-only' signal in single-molecule measurements *in vitro*.

Cell culture and microinjection. *Cell culture.* HeLa cells (American Type Culture Collection; mycoplasma free, tested with the MycoAlert mycoplasma detection Kit (Lonza); the identity of the cells was confirmed by visually inspecting the cell morphology) were cultured in tissue culture flasks (75 cm^2, TPP) in humid atmosphere at 37 °C and 5% CO_2. The cells were grown in phenol red–free Dulbecco's modified Eagle medium (DMEM, Invitrogen), supplemented with 10% FCS (Bioconcept Amimed), 100 units/ml penicillin, and 0.1 mg/ml streptomycin (Sigma). Cells were subcultured when approximately 80% confluency was reached using trypsin-EDTA (Sigma) for cell detachment. One day before a single-molecule experiment, 2×10^5 HeLa cells in 4 ml phenol red–free DMEM medium were pipetted into a microscopy dish (35-mm glass-bottom dishes, Ibidi) and incubated overnight (37 °C, 5% CO_2) until the cells became adherent again. Prior to single-molecule measurements, the medium was aspirated; the cells were then washed three times with Hanks balanced salt solution (HBSS, Sigma; HBSS contains 1.3 mM $CaCl_2$, 0.8 mM $MgSO_4$, 5.4 mM KCl, 0.44 mM KH_2PO_4, 4.2 mM $NaHCO_3$, 136.9 mM NaCl, 0.3 mM Na_2HPO_4 and 5.6 mM glucose) and covered with a buffer of choice. For experiments with different salt concentrations (up to 300 mM total ionic strength in the medium) or for temperature experiments, the microscopy dishes were first coated with poly(L-lysine) solution (0.01% in H_2O, Sigma) to improve cell adhesion.

Microinjection. Protein solutions were injected into HeLa cells using a Xenoworks microinjection system (Sutter Instrument), which was directly attached to the single-molecule fluorescence microscope. The pressure pulses (0.5–1 bar, 20–50 ms) for the injections were delivered by a home-built injector or a Picospritzer III (Parker). The sample was injected into cells using Femtotips II capillaries (Eppendorf). Before cell injection, the operational capability of the system was tested by injecting sample several times into the cell medium while recording a transfer efficiency histogram with the single-molecule fluorescence microscope. For all experiments with GB1 and Yfh1, the inside of the capillaries was first coated with 1 mg/ml poly(L-lysine)-*graft*-poly(ethylene glycol)[57] (PLL(20)-*g*[3.5]-PEG(2), SuSoS), dissolved in doubly distilled H_2O (ddH_2O), for 5 min, to reduce the adherence of the proteins to the glass capillary. Before loading the sample, which needs to be dissolved in a low-salt buffer to minimize dissociation of PLL-PEG—for example, 20 mM sodium phosphate buffer, pH 7.0—the coated capillaries were rinsed twice with ddH_2O. All protein samples for injections contained 0.005% Tween 20 (Pierce) to reduce adsorption of protein to any container surfaces used during dilution, and the sample was injected into either the cytosol or the nucleus of a targeted cell. Solutions for injection contained labeled protein at concentrations of ~20–50 nM. For every measurement, a single pressure pulse was applied to deliver the sample into the cell. The pressure settings and the duration of the pulses for the sample injections into HeLa cells were optimized in a way that (i) enough sample was injected to observe a sufficiently large number of fluorescence bursts per cell and (ii) the pressure pulse was gentle enough to avoid the formation of membrane protuberances or cell lysis, clear indications of compromised cellular viability (**Supplementary Fig. 12**). Slight adjustments of pressure pulses within the range given above were made for every set of measurements involving a stock solution of a given protein concentration. Longer-term cell viability after injection with parameters optimized in this way was assessed by adding propidium iodide[58] (Sigma) to the medium after injection of buffer into the cytosol of 23 HeLa cells (**Supplementary Fig. 1**). The membrane integrity and cell morphology were tracked up to 1.5 h after injection. Immediately after injection, all injected cells were still intact. After 1.5 h, 74% of all injected cells were still intact; four cells (18%) showed blebbing, and one cell was found dead according to the propidium iodide stain.

Instrumentation for single-molecule FRET in cells. *Single-molecule fluorescence microscope.* Single-molecule fluorescence measurements were performed on a custom-built confocal

instrument using an Olympus IX71 microscope body. Light from a 20-MHz supercontinuum laser (SC-450-4, Fianium) was used for excitation, with the wavelength selected via a 520/15 band-pass filter (Chroma Technology), and focused into the sample with an Olympus UplanApo 60×/1.20-W objective (Olympus). Photons emitted from the sample were collected through the same objective. Scattered excitation light was eliminated with a long-pass filter (LP532, Chroma Technology) before the emitted photons passed a 100-μm confocal pinhole. The emitted photons were then separated into four channels with a polarizing beam splitter and two dichroic mirrors (635DCXR, Chroma Technology). Donor photons were filtered (ET585/65m, Chroma Technology) and then focused on τ-SPAD avalanche photodiodes (PicoQuant). Acceptor photons were filtered (LP647RU and HC750/SP, Chroma Technology) and detected with SPCM-AQRH-14 single-photon avalanche diodes (PerkinElmer). The arrival times of detected photons were recorded with four channels of a HydraHarp 400 counting module (PicoQuant) with a resolution of 16 ps. All measurements were performed by exciting the donor dye with a laser power of 50 μW, measured at the back aperture of the objective. The objective was mounted on a piezo stage combination (P-733.2 and PIFOC, Physik Instrumente GmbH) to enable 3D scans. During such a scan, the sample was excited with pulsed laser light (20 MHz, 520 nm). The emitted fluorescence was used to generate fluorescence lifetime images of the scanned cells using the SymPhoTime software package (PicoQuant).

In-cell FRET and nanosecond FCS of ProTα. Single-molecule FRET efficiency histograms of ProTα in living cells were acquired by injecting samples with a protein concentration of 10 nM into the cytosol or nucleus of HeLa cells. ProTα was dissolved in the buffer used for the experiment, additionally containing 0.005% Tween 20. All experiments with ProTα were performed at 22 °C. As a sample buffer and extracellular medium, modified HBSS without Ca^{2+} and Mg^{2+} and with different NaCl concentrations was used. Besides NaCl, every buffer contained 0.3 mM Na_2HPO_4 (Sigma), 0.4 mM KH_2PO_4 (Sigma), 5.4 mM KCl (Sigma), 4.2 mM $NaHCO_3$ (Sigma) and 5.6 mM glucose (Sigma). The concentration of NaCl was adjusted to the desired final ionic strength of the buffer (30 mM, 80 mM, 137 mM, 280 mM and 980 mM NaCl), yielding buffers with total ionic strengths of 50 mM, 100 mM, 156 mM, 300 mM and 1,000 mM, respectively. The pH of the buffers was between 7.2 and 7.4. The cells were incubated in the corresponding buffer for 15 min before the sample was injected into the cells. For experiments with buffers with ionic strengths of 50 mM, 100 mM, and 156 mM, the microscopy dishes were coated with poly(L-lysine), for improved cell adhesion, before cells were added. Note that in the range of salt concentrations used here, no detectable effects on the stability and photophysics of the dyes are expected[32]. For I = 50 mM, 6 cytosolic and 1 nuclear measurements were performed; for I = 100 mM, 6 cytosolic and 8 nuclear measurements; for I = 156 mM, 8 cytosolic and 8 nuclear measurements; for I = 300 mM, 7 cytosolic and 8 nuclear measurements; for I = 1,000 mM, 5 cytosolic and 4 nuclear measurements. Each data point was collected in a different cell.

Two slightly different procedures were used for in-cell data acquisition. In both cases, before injection, a FLIM image of the cells was first taken in the axial direction for setting the z position, and then an image in the xy plane was recorded. After microinjection of sample into a few cells, success of injection was verified by recording a second FLIM image of the injected cells in the xy plane (for example, **Fig. 1b**), and the confocal volume was positioned either in the cytosol or the nucleus of the injected cells and away from regions of high cellular autofluorescence. Alternatively, in order to minimize photobleaching of the injected sample, we recorded an image of the cells only before injection, and the position of the confocal volume after injection was chosen on the basis of that image. The confocal spot was then set to the position of choice, either in the cytosol or in the nucleus of an injected cell. In both cases, positioning of the observation volume was additionally verified by the presence of fluorescence bursts (**Fig. 1c**) and the slower translational diffusion of the molecules compared to the extracellular medium (**Fig. 1d**). From each injected cell, data were acquired for 2–3 min until most of the injected protein was photobleached. The concentration of labeled protein in the injected cells was estimated by comparing the frequency of detected fluorescence bursts with reference measurements *in vitro* and yielded concentrations between 50 pM and 500 pM. (Note that at such low concentrations of injected sample, using the amplitudes of the component of FCS curves corresponding to translational diffusion for the determination of concentrations[6] is complicated by the contribution of cellular autofluorescence.)

Nanosecond FCS (nsFCS) measurements in cells were performed by injecting ProTα in HBSS without Ca^{2+} and Mg^{2+} (I = 156 mM), containing 0.005% Tween 20. Owing to the poorer photon statistics for interphoton times in the nanosecond range, the measurements require a substantially larger total number of photons to be detected than are needed for FRET efficiency histograms. Optimal signal-to-noise ratio is achieved in the range of ~1 nM of labeled protein; we thus injected correspondingly higher concentrations of labeled ProTα (20 nM). Injections and measurements were performed as described above. In contrast to the other single-molecule fluorescence measurements, nsFCS measurements were carried out using a 532-nm continuous-wave laser (LaserBoxx LMX-532S, Oxxius) at 100-μW excitation power, as measured at the back aperture of the objective. In-cell experiments were performed by measuring the fluorescence in each injected cell for 3 min. To achieve sufficient statistics, we averaged the results of 51 single-cell measurements, which resulted in a total acquisition time of 2.5 h. We note that, given the small cell-to-cell variation in $\langle E \rangle$, a large heterogeneity in dynamics seems unlikely. Also, during the measurement in one single cell, the transfer efficiency of ProTα remained constant to within experimental uncertainty (**Supplementary Fig. 13**). Control measurements in buffer were carried out with protein concentrations of 200 pM in HBSS with 0.001% Tween 20 for 12 h. Owing to the relatively low transfer efficiency of the ProTα variant used here and the limited signal-to-noise ratio, the amplitude of the cross-correlation component corresponding to chain dynamics is not detectable in our intracellular measurements (**Fig. 1f**).

In-cell FRET of Yfh1 at different temperatures. For intracellular measurements at different temperatures, a custom-made temperature-controlled cell-culture dish holder employing Peltier elements and a digital temperature controller (HAT Control-M20, BelektroniG GbR) with a Pt100 temperature sensor (**Supplementary Fig. 7**) was used. The Peltier elements were cooled by continuous water circulation. The microscope objective was temperature regulated using an aluminum collar to which a

doi:10.1038/nmeth.3475

water-cooled Peltier element was mounted[40]. For temperature-dependent control measurements in buffer, a custom-built temperature-controlled sample holder for glass cuvettes employing Peltier elements and a HAT Control-M20 temperature controller with a Pt100 temperature sensor was used as previously described[5]. For both extracellular and intracellular measurements, the temperature at the laser focus was calibrated using the temperature-dependent fluorescence lifetime of rhodamine B[40,59,60].

HeLa cells were grown in poly(L-lysine)-coated microscopy dishes. The cells were kept in HBSS without Ca^{2+} and Mg^{2+} salts (I = 156 mM). Yfh1 in cells was measured at temperatures between 279 K and 299 K. Above that temperature range, the pH became instable too quickly, which led to cell detachment (for measurements at higher temperatures, a CO_2 cabinet attached to the microscope would need to be employed to maintain the physiological pH). Nevertheless, HeLa cells were found to tolerate from ~277 K to ~303 K without loss of surface adherence after microinjection. A 50 nM Yfh1 solution in 20 mM sodium phosphate buffer, pH 7.0, and 0.005% Tween 20 was injected into HeLa cells with PLL-PEG–coated glass capillaries. Extracellular measurements were performed with 50 pM Yfh1 in 50 mM sodium phosphate buffer, pH 7.0, in HBSS and in HBSS without Ca^{2+} and Mg^{2+}. Every buffer additionally contained 144 mM β-mercaptoethanol and 0.001% Tween 20, and measurements were performed at different temperatures (for measurement in HBSS buffer, see **Supplementary Fig. 8**). The measurements at 279 K were performed in 8 individual cells, at 282 K in 11 cells, at 286 K in 8 cells, at 289 K in 10 cells, at 293 K in 10 cells, and at 299 K in 12 cells. Note that in the temperature range accessible here, only minor effects on the stability and photophysics of the dyes are expected[40,59,61]. Both here and in the cases of ProTα and GB1, some variation in the amplitudes of the donor-only peak from cell to cell was observed. Given the absence of donor-only bursts in noninjected cells (**Supplementary Fig. 14**), the most likely reasons of this variation are photobleaching and/or differences in intracellular proteolytic degradation.

Recurrence analysis of single particles (RASP) with GB1 in the cell. RASP is based on the observation that at sufficiently low sample concentrations and for timescales up to several tens of milliseconds, the probability that a fluorescently labeled molecule returns to the confocal volume is greater than the probability of a new molecule being detected[43]. Intramolecular interconversion kinetics can then be quantified by the changes in transfer efficiency histograms obtained from fluorescence bursts detected within a defined time interval that is varied systematically (**Supplementary Fig. 10**). The possibility of extracting kinetics for times longer than the diffusion time through the confocal volume (~1 ms) critically depends on the probability that two fluorescence bursts separated by a time τ were emitted by the same molecule ($p_{same}(\tau)$). For the large sample volumes used in typical *in vitro* single-molecule measurements, the huge reservoir of fluorescent molecules (~10^9) leads to a rapid drop of p_{same} with increasing τ (ref. 43). However, owing to the confinement within the small cellular volume (~0.5 pl), p_{same} remains high for much longer times, as illustrated by simulations (**Fig. 4b**). Essentially, cellular confinement strongly increases the probability of observing multiple transits of a molecule through the confocal volume, which extends the effective observation time and makes recurrence analysis ideally suited for probing intracellular conformational dynamics.

RASP measurements in cells were performed at 4 °C to improve the peak separation between the unfolded and folded population (as in the case of Yfh1 (ref. 40), the unfolded state expands with decreasing temperature, resulting in lower transfer efficiency and thus better separation from the high-transfer-efficiency folded peak). For intracellular measurements, the temperature-controlled cell-culture dish holder and the objective collar were used as described above. Adherent HeLa cells for in-cell RASP experiments were grown in microscopy dishes, as described above. The medium was decanted, and the cells were washed three times with HBSS and cooled to 4 °C. Microinjection was performed using a 20 nM GB1 solution in PLL-PEG–coated glass capillaries. GB1 was injected into the cytosol of 61 HeLa cells, and fluorescence bursts were collected for 5 min per cell. To maximize throughput, we verified successful injection not by detailed fluorescence imaging but by the appearance of fluorescence bursts upon placing the confocal volume inside the cytoplasm and the reduced translational diffusion time of molecules inside cells compared to the extracellular medium. Buffer measurements were carried out in 50 mM sodium phosphate buffer, pH 7.0, 144 mM β-mercaptoethanol, and 0.001% Tween 20. Single-molecule FRET histograms in buffer were acquired in samples with a protein concentration of 20 pM. The protein concentration was chosen low enough to maximize the same-molecule probability, $p_{same}(\tau)$, i.e., the probability that two fluorescence bursts, separated by a short time τ (up to 100 ms), are emitted by the same molecule that happens to return to the confocal volume. As a consequence of the low protein concentrations, fluorescence bursts had to be collected for over 20 h *in vitro* to obtain sufficient statistics for a robust analysis of the exchange dynamics between folded and unfolded states[43].

Simulation of RASP data. For a better understanding of the shape of the $p_{same}(\tau)$ curve obtained from the measured data, we simulated trajectories of particles labeled with one fluorophore freely diffusing (diffusion coefficient $D = 1 \times 10^{-5}$ μm²/μs) in the confined volume of a living cell, which we approximated by a flat cylinder of diameter d = 20 μm and height h = 1, 2, 4 or 10 μm. Trajectories were simulated for each particle as a random walk with step sizes in each spatial direction drawn from a normal distribution with variance $\sigma^2 = 2D\Delta$, where Δ = 1 μs is the time between two steps. We approximate the dependence of the fluorescence photon rate n on the position (x, y, z) inside the confocal volume by a 3D Gaussian

$$n(x,y,z) = n_0 e^{-2(x^2+y^2)/\omega_1^2} e^{-2z^2/\omega_2^2}$$

with ω_1 = 0.15 μm, ω_2 = 0.9 μm, and n_0 = 0.4 photons/μs. The probability of photobleaching during one simulation step is given by $p_{bleach} = \alpha_{bleach} n(x, y, z)\Delta$ with α_{bleach} = 0.0025. Initially (t = 0), N particles were randomly distributed inside the cylinder. Each particle trajectory was simulated for 180 s or until bleaching of the fluorophore, whichever occurred first. Finally, for all times t, the combined fluorescence emission rate of all particles, $n_{tot}(t)$, was calculated, and photon-detection events as a function of time were simulated with mean interphoton times given by $1/n_{tot}(t)$. The simulated photon trajectories were then analyzed in the same way as the measured fluorescence data to obtain the $p_{same}(\tau)$ curves presented in **Figure 4b**.

Microfluidic mixing. Microfluidic mixing experiments were performed to independently test the unfolding and folding kinetics of GB1 determined by recurrence measurements using RASP[43]. Microfluidic devices were fabricated using replica molding in poly(dimethylsiloxane) (PDMS) as described previously[62]. In concordance with the RASP measurements, microfluidic experiments were performed at 4 °C. To reach this temperature inside the microfluidic mixing device, both the microscope objective and the microfluidic device holder[62] were cooled to 1.00 °C and 0.25 °C, respectively. The actual temperature inside the microfluidic channels was confirmed by measuring the fluorescence lifetime of a 1 μM rhodamine B solution[60] (excitation power, 0.06 μW at 532 nm with 20-MHz repetition rate). To minimize surface adhesion of fluorescently labeled protein to the channel walls, we flushed microfluidic mixing devices with an aqueous solution of 0.1 mg/ml PLL(20)-g[3.5]-PEG(2) for 1 h before the actual mixing experiment. Refolding experiments were performed in the microfluidic mixing device by jumping GB1 from 800 mM to 80 mM GdmCl (**Supplementary Fig. 9**). To determine the folding-unfolding rate of GB1 starting from an ensemble biased toward the unfolded state, the center inlet of the microfluidic mixing device was filled with sample containing 250 pM GB1 in 50 mM sodium phosphate buffer with 800 mM GdmCl, 140 mM β-mercaptoethanol and 0.01% Tween 20, pH 7. Side inlets were filled with 50 mM sodium phosphate buffer, pH 7. Application of 23.4 kPa and 24.8 kPa to the center and side inlets resulted in an average flow velocity of 1 mm/s, a mixing ratio of 1:10, and a concentration of 25 pM GB1 in 80 mM GdmCl in the observation channel. Note that the pressures necessary are substantially higher than those previously reported[62] owing to increased viscosities at 4 °C, as measured using a digital viscometer (DV-I+, Brookfield).

Kinetic series were obtained by acquiring transfer efficiency histograms at different positions along the observation channel, corresponding to different times after mixing. 50 μW of excitation power of a 532-nm continuous-wave laser (LaserBoxx LMX-532S, Oxxius) were used. Transfer efficiency histograms were recorded for 5 min per data point. Three sets of measurements were averaged, and for the estimation of error bars, we assumed the uncertainties to be uniformly distributed. Positions along the observation channel were converted into times after mixing as described previously[63]. Positions corresponding to short times after mixing (up to 50 ms) were accessed using a piezo stage combination (P-733.2 and PIFOC, PI) and those for longer times were accessed using the manual translation stage of the microscope. Histograms were obtained from 2.1 ms to 377 ms after mixing.

Data analysis. *Transfer efficiency histograms.* Fluorescence bursts from individual molecules were identified by combining successive photons separated by interphoton times of less than 100 μs and retained as a burst if the total number of photons detected was larger than a threshold of 30–50, chosen depending on the intensity of the background signal. The background was variable during a measurement owing to photobleaching and was quantified by splitting the time traces into short intervals where the background could be assumed to be constant. Detected bursts from each interval were summed up to construct the final transfer efficiency histogram. The transfer efficiency of each burst was calculated according to $E = n_A/(n_A + n_D)$, where n_D and n_A are the numbers of donor and acceptor photons, respectively, corrected for background in the corresponding interval, acceptor direct excitation, channel cross-talk, differences in detector efficiencies, and quantum yields of the dyes as previously described[64]. (Note that owing to these corrections, E values >1 and <0 are possible in the transfer efficiency histograms.)

For all three proteins investigated here, the 'donor-only' population (i.e., the fraction of fluorescence bursts from molecules lacking an active acceptor dye with an apparent transfer efficiency close to 0) is larger for in-cell measurements than for *in vitro* measurements. Several indications suggest that this signal originates from a preferential inactivation of the acceptor dye in the cell or from cellular degradation of part of the injected molecules, as follows. (i) The yield of correctly FRET-labeled molecules for all samples was >90% (see "Protein expression and labeling"), which is reflected by the small donor-only population in *in vitro* measurements (**Figs. 1e** and **4c** and **Supplementary Fig. 8**). (ii) Measurements in noninjected cells analyzed with the thresholds of our in-cell measurements yielded a negligible signal in the transfer efficiency range of the donor-only peak (**Supplementary Fig. 14**). (iii) The fluorescence lifetime of the donor-only population was not significantly different from the donor lifetime in extracellular measurements (**Supplementary Fig. 5**), suggesting that the donor-only signal does not originate from cellular autofluorescence, which exhibits a different lifetime (**Fig. 1b** and **Supplementary Fig. 3**). (iv) The lower number of fluorescence bursts with a transfer efficiency close to 0 upon scanning the sample compared to stationary measurements (**Supplementary Fig. 4**) indicates the contribution of photobleaching to the donor-only population.

Fitting of transfer efficiency histograms. To analyze subpopulations in transfer efficiency histograms, we approximated peaks in the histograms with Gaussian (G) and four-parameter log-normal (L) peak functions for symmetric and asymmetric peaks, respectively:

$$G(E) = Ae^{-\frac{(E-E_0)^2}{2w^2}}$$

and

$$L(E) = A\exp\left(-\frac{\ln(2)}{\ln(a)^2}\ln\left(1+\frac{a^2-1}{aw}(E-E_0)\right)^2\right)$$

with E being the transfer efficiency, A the peak amplitude, E_0 the peak position, w the peak width, and a the asymmetry of the peak[65–67]. For fitting more than one peak, the histogram was analyzed with a sum of peak functions. In many cases where several histograms contained peaks from the same species, the peaks were described with a global fit over all histograms, with E_0, w, and/or a for some subpopulations as shared or fixed parameters (amplitudes were never constrained). Where necessary, the choice of fixed parameter values was based on histograms where the respective peaks were as well defined as possible (i.e., separated from other subpopulations and/or with the best available statistics, or from recurrence histograms in the case of GB1).

doi:10.1038/nmeth.3475

Specifically, transfer efficiency histograms of ProTα (**Figs. 1** and **2** and **Supplementary Fig. 13**) were fitted using a log-normal peak function for the donor-only population with a fixed width (0.15) and asymmetry (1.32). These values were chosen to best describe the observed shape of the donor-only population. The FRET-labeled population was fitted with a Gaussian peak function without constraints of fit parameters.

Transfer efficiency histograms of frataxin (**Fig. 3** and **Supplementary Fig. 8**) were fitted globally using a log-normal peak function for the donor-only population, with a fixed width (0.14 *in vitro*, 0.2 *in vivo*), and asymmetry (1.1 *in vitro*, 1.4 *in vivo*); the position was a fit parameter shared by all histograms of the respective data set. These values were chosen to best describe the observed shape of the donor-only population. The unfolded population was fitted with a Gaussian peak function using the width as a fit parameter shared by all histograms in the case of **Supplementary Figure 8** and, owing to the lower statistics, with a width fixed to 0.09 in case of **Figure 3**. The folded population was fitted with a Gaussian peak function using the width as a global fit parameter for all histograms in the case of **Supplementary Figure 8** and with fixed width (0.09) in case of **Figure 3**. In the case of **Figure 3**, the position of the native population was a fit parameter shared by all histograms (based on the assumption that the transfer efficiency of the folded population is virtually constant over this temperature range, as *in vitro*). The widths of the unfolded and folded populations *in vivo* (0.09) were chosen on the basis of observations made with ProTα and GB1, for which a slight broadening of peaks was observed compared to *in vitro*.

Transfer efficiency histograms of GB1 (**Fig. 4** and **Supplementary Figs. 9** and **10**) were fitted globally using a log-normal peak function for the donor-only and folded populations and using a Gaussian peak function for the unfolded population. In all cases, the donor-only population was fitted with fixed position (−0.03), width (0.14), and asymmetry (1.09). All parameters for the donor-only, folded, and unfolded subpopulations (and for ProTα in the control) were obtained from globally fitting the early-time recurrence histograms of each population without any constraints but using p, w, and a of the respective populations as shared parameters; the results from these fits were used to fix the parameters in the remaining recurrence histograms. Correspondingly, the unfolded population was fitted with a fixed position (0.85) and width (0.08 *in vitro*, 0.1 *in vivo*) (based on ΔE = (0.7–0.9) and ΔT = (0–1 ms)). The native population was fitted with a fixed position (1.0), width (0.07 *in vitro*, 0.09 *in vivo*), and asymmetry (0.42 *in vitro*, 0.63 *in vivo*) (based on ΔE = (0.95–1.1) and ΔT = (0–1 ms)). The histograms shown in **Supplementary Figure 11** were fitted with fixed position (−0.05), width (0.13), and asymmetry (1.17) for the donor-only population (log-normal peak). The population of ProTα (Gaussian peak) was fitted with fixed position (0.43) and width (0.1) (based on ΔE = (0.35–0.55) and ΔT = (0–5 ms)). The population of GB1 wild type was fitted with fixed position (1.0), width (0.09), and asymmetry (0.76), using log-normal peak functions (based on ΔE = (0.9–1.1) and ΔT = (0–5 ms)).

Interdye distances and radii of gyration. Dimensions of unfolded/intrinsically disordered proteins were calculated from the measured transfer efficiencies as described earlier[66]. Briefly, the mean transfer efficiency, $\langle E\rangle$, can be expressed as a function of the distance dependence of the transfer efficiency, $E(r)$, weighted for the dye-to-dye distance distribution, $P(r)$, sampled by the chain,

$$\langle E\rangle = \int_a^{l_c} E(r)P(r)\mathrm{d}r$$

with

$$E(r) = \frac{1}{1+(r/R_0)^6}$$

where a is the distance of closest approach of the two dyes, l_c is the contour length of the labeled protein segment, and R_0 is the Förster radius of the chosen dye pair. To enable a direct comparison with previous experiments *in vitro*[32,40,66], we assumed a simple Gaussian chain model for the distribution of distances, $P(r)$,

$$P(r) = 4\pi r^2\left(\frac{3}{2\pi\langle r^2\rangle}\right)^{3/2}\exp\left(-\frac{3r^2}{2\langle r^2\rangle}\right)$$

where $\langle r^2\rangle$ is the mean squared interdye distance. These equations were solved for $\langle r^2\rangle$ numerically and then converted to the mean radius of gyration, R_g, of the chain using

$$R_g^2 = \frac{1}{6}\langle r^2\rangle.$$

We note that a systematic uncertainty in the Förster radius propagates linearly to $\langle r^2\rangle^{1/2}$ and thus introduces a systematic uncertainty in the absolute values of R_g. However, as we only compare measurements between identical samples under different conditions, this contribution is not considered here.

Fluorescence anisotropy values of donor emission of all samples were in the range of 0.04–0.11 *in vitro* and 0.10–0.17 in in-cell experiments, as quantified on the basis of the polarization selectivity of our single-molecule measurements (**Supplementary Fig. 6**), supporting the approximation $\kappa^2 = 2/3$ used for the calculation of the Förster radii. Donor fluorescence lifetimes of ProTα in the absence of energy transfer resulted in values of 3.8 ns in buffer, 3.8 ns in the cytosol, and 3.9 ns in the nucleus (**Supplementary Fig. 5**), indicating only minor effects of the respective environment on the quantum yield and photophysics of the donor dye.

Fluorescence correlation spectroscopy. To extract the diffusion time of the labeled proteins, we correlated[25] the fluorescence intensity fluctuations measured in FRET experiments according to

$$g_{ij}(\tau) = \frac{\langle \delta n_i(0)\delta n_j(\tau)\rangle}{\langle n_i\rangle^2}$$

with i, j = A, D and where $n_i(0)$ and $n_j(\tau)$ are the fluorescence count rates for channels i and j at time 0 and after a lag time τ, respectively, and $\delta n_{i,j} = n_{i,j} - \langle n_{i,j}\rangle$ are the corresponding deviations from the mean count rates. The duration of the single-cell FRET measurements allows correlations to be calculated to a minimum lag time of 10^{-5} s, with sufficient photon statistics to quantify the photophysics of the triplet state and the translational

diffusion time of the molecule through the confocal volume. The resulting cross-correlation curves were fitted with[68]

$$g_{AD}(\tau) = 1 + \frac{1}{N_{AD}} \frac{1 + c_T^{(AD)} e^{-|\tau|/\tau_T^{(AD)}}}{(1 + |\tau|/\tau_D)(1 + |\tau|/s^2\tau_D)^{1/2}}$$

where the term in the numerator describes triplet blinking with amplitude c_T and a decay time τ_T. The denominator describes the diffusion of a protein through the confocal volume, with N_{AD} denoting the mean number of doubly labeled protein molecules in the confocal volume, s the ratio of axial over lateral radius of the confocal volume, and τ_D the translational diffusion time.

nsFCS. Donor and acceptor autocorrelation curves and cross-correlation curves between acceptor and donor channels were calculated as described earlier[25,69]. The resulting auto- and cross-correlation curves were fitted globally up to a delay time of 1 μs using

$$g_{ij}(\tau) = 1 + \frac{1}{N}\left(1 - c_{AB}e^{-|t - t_0|/\tau_{AB}}\right)\left(1 + c_{CD}e^{-|t - t_0|/\tau_{CD}}\right)\left(1 + c_T e^{-|t - t_0|/\tau_T}\right)$$

with i, j = A, D and with N denoting the mean number of proteins in the confocal volume. The three multiplicative terms describe photon antibunching (AB), chain dynamics (CD), and triplet blinking (T) of the dyes. τ_{CD} was extracted from the global fit of all three correlations (with τ_{CD} as a shared fit parameter) to quantify chain reconfiguration dynamics of ProTα.

RASP analysis. The fluorescence signal from the first 50 s of data acquisition in each cell showed a significant drop in signal in both donor and acceptor channels because of photobleaching and was excluded from the analysis. The fluorescence bursts identified in the remaining 250 s for 61 individual HeLa cells were combined and then subjected to RASP analysis. RASP analysis and the calculation of the p_{same} function from the burst time correlation function was carried out as described previously[43]. p_{same} can, under equilibrium conditions, be calculated from the time correlation of burst events, $g_{bursts}(\tau)$, by the equation $p_{same}(\tau) = 1 - 1/g_{bursts}(\tau)$. Inside the cells, however, we observe a decrease of fluorescent particle concentration over time caused by photobleaching, which means that for a given τ, $p_{same}(\tau)$ is increasing over time. Hence, the $p_{same}(\tau)$ calculated by the equation above from all observed bursts is only an average value. Recurrence FRET efficiency histograms were obtained by first selecting photon bursts from a small transfer efficiency range (ΔE = (0.7–0.9) for selecting mainly unfolded GB1; ΔE = (0.95 – 1.1) for selecting mainly folded GB1) and then building the FRET efficiency histogram only from bursts detected within a short time (the recurrence interval, T; **Supplementary Fig. 10**) after those initial bursts. Systematic variation of the recurrence interval allows the kinetics of interconversion between the subpopulations to be determined essentially in a model-free manner[43]. Note that the choice of the initial transfer efficiency range does not affect the relaxation time but only the amplitude of the transient observed[43] (**Supplementary Fig. 15**). The fractions of folded molecules from recurrence FRET efficiency histograms starting from unfolded (ΔE_1) and folded molecules (ΔE_2) using recurrence analysis over a 50-ms time window were fitted with a model including the folding-unfolding dynamics of recurring molecules, which allows the relaxation time of this process to be extracted[43]. The equilibrium constant was obtained from the ratio of unfolded and folded fractions from the total transfer efficiency histogram of a RASP measurement (**Fig. 4**).

Microfluidic mixing. Detected photons were binned into windows of 1 ms, and corrections for background, differences in quantum yields of the dyes, detection efficiencies, and cross-talk were applied. Bursts were identified using a threshold for the total number of detected photons per bin. Given the pronounced decrease in flow velocity in the first part of the observation channel corresponding to the entrance length, the threshold was varied as a function of the flow velocity from 21 photons per bin for the first recorded data point to 35 photons per bin for longer times after mixing to account for the differences in residence time. Transfer efficiency histograms show three peaks, corresponding to molecules lacking an active acceptor dye, unfolded GB1 (E = 0.86) and folded GB1 (E = 0.99), respectively. Histograms were fitted globally with a Gaussian and a log-normal peak function for the unfolded and folded populations, respectively; peak positions and widths were set as shared parameters and amplitudes fitted individually. The fraction of folded molecules was calculated from the relative area of the folded peak as obtained from the fits. The relaxation time of folding was extracted from a single exponential fit to the mean of three measurements. The equilibrium constant, K_{eq}, for the final conditions was obtained from a transfer efficiency histogram of GB1 measured in a cuvette in 50 mM sodium phosphate buffer with 80 mM GdmCl, 140 mM β-mercaptoethanol, and 0.01% Tween 20, pH 7. K_{eq} and the relaxation time from the mixing experiment were extrapolated to 0 M GdmCl using an m-value for folding of 1.5 kcal/mol/M and an m-value for unfolding of 0.4 kcal/mol/M. The m-values were average values taken from m-values of the single mutants F30L and G41A and wild-type GB1 (ref. 56).

Code availability. Data analysis was performed with a custom module for Mathematica (Wolfram Research), which is available upon request.

48. van de Linde, S., Heilemann, M. & Sauer, M. Live-cell super-resolution imaging with synthetic fluorophores. *Annu. Rev. Phys. Chem.* **63**, 519–540 (2012).
49. Raj, A. & van Oudenaarden, A. Nature, nurture, or chance: stochastic gene expression and its consequences. *Cell* **135**, 216–226 (2008).
50. Costantini, L.M., Fossati, M., Francolini, M. & Snapp, E.L. Assessing the tendency of fluorescent proteins to oligomerize under physiologic conditions. *Traffic* **13**, 643–649 (2012).
51. Plochowietz, A., Crawford, R. & Kapanidis, A.N. Characterization of organic fluorophores for *in vivo* FRET studies based on electroporated molecules. *Phys. Chem. Chem. Phys.* **16**, 12688–12694 (2014).
52. Kolmakov, K. *et al.* Red-emitting rhodamines with hydroxylated, sulfonated, and phosphorylated dye residues and their use in fluorescence nanoscopy. *Chemistry* **18**, 12986–12998 (2012).
53. Zanetti-Domingues, L.C., Tynan, C.J., Rolfe, D.J., Clarke, D.T. & Martin-Fernandez, M. Hydrophobic fluorescent probes introduce artifacts into single molecule tracking experiments due to non-specific binding. *PLoS ONE* **8**, e74200 (2013).
54. Yi, S., Brickenden, A. & Choy, W.Y. A new protocol for high-yield purification of recombinant human prothymosin alpha expressed in *Escherichia coli* for NMR studies. *Protein Expr. Purif.* **57**, 1–8 (2008).
55. Gronenborn, A.M. *et al.* A novel, highly stable fold of the immunoglobulin binding domain of streptococcal protein G. *Science* **253**, 657–661 (1991).

doi:10.1038/nmeth.3475

56. McCallister, E.L., Alm, E. & Baker, D. Critical role of β-hairpin formation in protein G folding. *Nat. Struct. Biol.* **7**, 669–673 (2000).
57. Kenausis, G.L. *et al.* Poly(L-lysine)-*g*-poly(ethylene glycol) layers on metal oxide surfaces: attachment mechanism and effects of polymer architecture on resistance to protein adsorption. *J. Phys. Chem. B* **104**, 3298–3309 (2000).
58. Nicoletti, I., Migliorati, G., Pagliacci, M.C., Grignani, F. & Riccardi, C. A rapid and simple method for measuring thymocyte apoptosis by propidium iodide staining and flow cytometry. *J. Immunol. Methods* **139**, 271–279 (1991).
59. Nettels, D. *et al.* Single-molecule spectroscopy of the temperature-induced collapse of unfolded proteins. *Proc. Natl. Acad. Sci. USA* **106**, 20740–20745 (2009).
60. Benninger, R.K. *et al.* Quantitative 3D mapping of fluidic temperatures within microchannel networks using fluorescence lifetime imaging. *Anal. Chem.* **78**, 2272–2278 (2006).
61. Wuttke, R. *et al.* Temperature-dependent solvation modulates the dimensions of disordered proteins. *Proc. Natl. Acad. Sci. USA* **111**, 5213–5218 (2014).
62. Wunderlich, B. *et al.* Microfluidic mixer designed for performing single-molecule kinetics with confocal detection on timescales from milliseconds to minutes. *Nat. Protoc.* **8**, 1459–1474 (2013).
63. Wunderlich, B., Nettels, D. & Schuler, B. Taylor dispersion and the position-to-time conversion in microfluidic mixing devices. *Lab Chip* **14**, 219–228 (2014).
64. Schuler, B., Müller-Späth, S., Soranno, A. & Nettels, D. Application of confocal single-molecule FRET to intrinsically disordered proteins. *Methods Mol. Biol.* **896**, 21–45 (2012).
65. Schuler, B., Lipman, E.A. & Eaton, W.A. Probing the free-energy surface for protein folding with single-molecule fluorescence spectroscopy. *Nature* **419**, 743–747 (2002).
66. Hoffmann, A. *et al.* Mapping protein collapse with single-molecule fluorescence and kinetic synchrotron radiation circular dichroism spectroscopy. *Proc. Natl. Acad. Sci. USA* **104**, 105–110 (2007).
67. Kuzmenkina, E.V., Heyes, C.D. & Nienhaus, G.U. Single-molecule Forster resonance energy transfer study of protein dynamics under denaturing conditions. *Proc. Natl. Acad. Sci. USA* **102**, 15471–15476 (2005).
68. Zander, C., Enderlein, J. & Keller, R.A. *Single Molecule Detection in Solution: Methods and Applications* (Wiley, 2003).
69. Nettels, D., Hoffmann, A. & Schuler, B. Unfolded protein and peptide dynamics investigated with single-molecule FRET and correlation spectroscopy from picoseconds to seconds. *J. Phys. Chem. B* **112**, 6137–6146 (2008).